Dislocation image on x-ray topographs within kinematical theory

Izumi Iwasa*

Fuji Xerox Co., Ltd., Nakai-machi, Kanagawa 259-0157, Japan

X-ray topographs of perfect crystals and dislocated crystals have been calculated within kinematical theory. The dislocation image on a x-ray topograph is found to be a circle, a ridge, or a trench depending on the type of dislocation and diffraction condition. Its radius or width is comparable to the radius of the first Fresnel zone, $r_1 = \sqrt{\lambda x_0}$, where λ is the wavelength of the x rays and x_0 is the distance from the crystal to the observation point. The Fresnel model is applied to the x-ray topograph of solid helium. r_1 is estimated to be 2.8 μm. The different contrast of the subboundaries appearing on the x-ray topographs of solid helium is explained in terms of the contrast of the dislocation images based on the calculation.

I. INTRODUCTION

The x-ray topography is a useful means for studying dislocations and other defective structures in crystalline materials. The x-ray diffraction from high-quality crystals of ordinary materials such as metals and semiconductors, in which the extinction distance is much shorter than the thickness of the specimen and multiple diffraction of the incident x rays occurs, is described by the dynamical theory.[1] In this case, dislocations can be observed in the x-ray topographs, because the diffraction condition around a dislocation is different from the other part of the crystal and multiple diffraction is reduced.

Solid helium exists only under pressure (above 2.5 MPa in the case of ^{4}He) at low temperatures down to 0 K because of the large zero-point energy, so that the density of a helium crystal grown in a pressurized cell is expected to be almost uniform with no macroscopic voids and cracks. Possible lattice defects in single crystals of solid helium are vacancies, isotopic impurities, and dislocations. Formation energies and activation energies of the vacancy in bcc ^{3}He have been determined by the specific-heat,[2] pressure,[3] x-ray[4] and NMR (Ref. 5) measurements. Existance of dislocations have been indicated in the ultrasonic measurements on hcp ^{4}He,[6] bcc and hcp ^{3}He,[7] and the experiments of plastic deformation.[8,9] It has been poined out from the amplitude dependence of sound attenuation in bcc ^{3}He, (Ref. 10) that quantum mechanical tunneling of dislocations may happen. Hence, direct observation of dislocations in solid helium is desirable to understand the mechanical properties of solid helium more deeply.

Recently, synchrotron-radiation x-ray topographs of hcp ^{4}He crystals have revealed the existance of tilt subboundaries in solid helium.[11] The size of the subgrains is of the order of 1 mm. The subboundaries are found to be perpendicular to the basal plane of the hexagonal crystal and to comprize basal edge dislocations. However, individual dislocations have not been identified in the topographs of the helium crystals.

Helium atoms are very weak x-ray scatterers. The atomic scattering factor is proportional to the number of orbital electrons which is 2 for the helium atom. Moreover, solid helium is called a quantum crystal because the amplitude of the zero-point vibration in the helium crystals amounts as much as 30% of the interatomic distance.[12] The zero-point vibration in turn reduces the intensity of the coherent diffraction of x rays drastically via the Debye-Waller factor. As a result, the extinction distance of x rays in solid helium is estimated to be as long as 2.5 mm,[13] which is greater than the size of the subgrains. Hence, the x-ray diffraction from helium crystals is supposed to be described not by the dynamical theory but by the kinematical theory, in which the incident beam is diffracted only once by the atoms and multiple diffraction is neglected.

The images of dislocations in the transmission electron microscope were theoretically calculated by Hirsch *et al.* based on kinematical theory.[14] They used the columnar approximation, in which the amplitude of diffraction at a point *P* below the sample was calculated as a sum of the diffracted waves from the atoms in a single column of unit cells in the diffraction direction. In the case of x-ray diffraction, however, the columnar approximation is not adequate. Diffracted waves from the atoms in a wider region than a column must be taken into account, because the wavelength of x rays (typically 0.1 nm) is much longer than that of the electron (0.0037 nm at 100 keV). Therefore, we need to calculate the dislocation images in the x-ray topographs based on kinematical theory more rigorously than the columnar approximation.

The purpose of this paper is to calculate the amplitude and intensity of the diffracted x rays from model crystals within the kinematical theory and to estimate the dislocation image on the x-ray topograph. The model crystals and kinematical theory are described in Secs. II and III, respectively. We study the x-ray diffraction from the perfect crystals in Sec. IV and that from the crystals with a dislocation in Sec. V. Then the experimental results on the x-ray topography of solid helium are presented in Sec. VI. Finally we discuss the images of various dislocations on the topographs and compare them with the x-ray topographs of solid helium in Sec. VII.

II. MODEL CRYSTALS

The model for the perfect crystal is of simple cubic structure with a lattice constant $a = 1$. The crystallographic axes
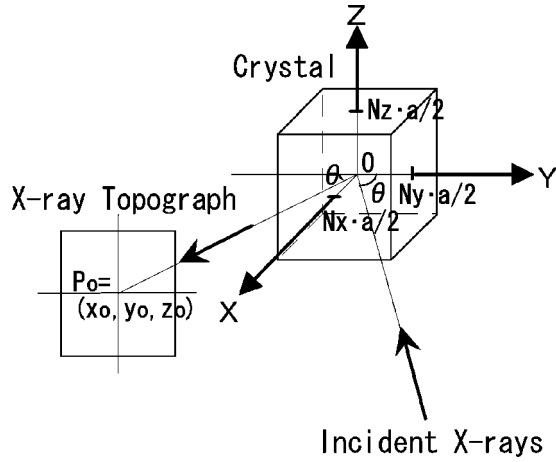
FIG. 1. Geometry of the crystal and x rays for the calculation of x-ray topographs.

are parallel to the x, y, and z directions of the Cartesian coordinate system. The numbers of atoms in the x, y, and z directions are N_x, N_y, and N_z, respectively. The total number of the atoms is given by

$$N = N_x \times N_y \times N_z. \tag{1}$$

The center of the crystal is taken as the origin of the coordinate system. The position of the jth atom is given by

$$\mathbf{r}_j = \mathbf{r}_{\alpha\beta\gamma} = (\alpha a, \beta a, \gamma a), \tag{2}$$

where α, β, and γ are integers or half integers with N_x, N_y, and N_z being odd or even, respectively. For example, α is given by

$$\alpha = -\frac{N_x - 1}{2}, -\frac{N_x - 1}{2} + 1, \ldots, \frac{N_x - 1}{2}. \tag{3}$$

The crystal occupies a region of

$$|x| \leq \frac{N_x a}{2}, \quad |y| \leq \frac{N_y a}{2}, \quad |z| \leq \frac{N_z a}{2}, \tag{4}$$

as shown in Fig. 1.

A crystal with a dislocation line (hereafter called a dislocated crystal) is formed from the perfect crystal by introducing a straight dislocation line along the x, y, or z axis. The direction of the Burgers vector is parallel or antiparallel to the x, y, or z direction, and its magnitude b is equal to the lattice constant a. Altogether, 6 kinds of dislocated crystals with screw dislocations and 12 kinds of dislocated crystals with edge dislocations are considered as listed in Table I.

The displacements of the atoms, $\mathbf{u} = (u, v, w)$, in the dislocated crystals are calculated according to elasticity theory.[15] Although the size of the model crystal is small, we neglect the effect of image dislocations for simplicity.

In the case of a straight screw dislocation along the x axis ($l\|x$, $b\|x$; No. 1 in Table I), where l denotes the direction of the dislocation line and b the direction of the Burgers vector, the displacement of an atom at (x,y,z) is given by

TABLE I. Model crystals with a dislocation line and their image of dislocation on the x-ray topograph.

No.	l	b	Disl. type	Disl. image	Width
1	x	x	screw	circular	6.0
2	x	$-x$	screw	circular	6.0
3	x	y	edge	none	–
4	x	$-y$	edge	none	–
5	x	z	edge	none	–
6	x	$-z$	edge	none	–
7	y	x	edge	trench	5.5
8	y	$-x$	edge	trench	5.5
9	y	y	screw	none	–
10	y	$-y$	screw	none	–
11	y	z	edge	trench	6.0
12	y	$-z$	edge	ridge	5.0
13	z	x	edge	trench	5.5
14	z	$-x$	edge	trench	5.5
15	z	y	edge	trench	6.0
16	z	$-y$	edge	ridge	5.0
17	z	z	screw	none	–
18	z	$-z$	screw	none	–

$$u = \frac{b}{2\pi}\tan^{-1}\frac{z}{y}, \quad v = w = 0. \tag{5}$$

In Eq. (5), $\tan^{-1}(z/y)$ is defined to vary from $-\pi$ to π with the discontinuity occurring at $y < 0$ and $z = 0$. The position of each atom in the dislocated crystal is given by

$$\mathbf{r}_j = (\alpha a + u, \beta a + v, \gamma a + w). \tag{6}$$

The shape of the crystal with a screw dislocation $l\|x$, $b\|x$ is shown schematically in Fig. 2(a).

In the case of a straight edge dislocation along the x axis with the Burgers vector parallel to the y axis ($l\|x$, $b\|y$; No. 3 in Table I), the displacement of an atom at (x,y,z) is given by

$$u = 0, \tag{7a}$$
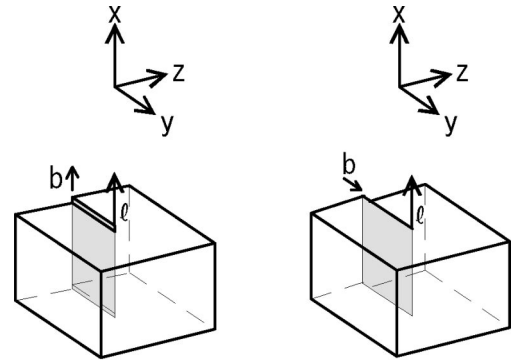
(a) l//x, b//x   (b) l//x, b//y

FIG. 2. Model crystals including (a) a screw dislocation $l\|x$, $b\|x$ and (b) an edge dislocation $l\|x$, $b\|y$.

$$v = \frac{b}{2\pi}\left[\tan^{-1}\frac{z}{y} + \frac{yz}{2(1-\nu)(y^2-z^2)}\right], \quad (7b)$$

$$w = -\frac{b}{2\pi}\left[\frac{1-2\nu}{4(1-\nu)}\ln(y^2+z^2) + \frac{y^2-z^2}{4(1-\nu)(y^2+z^2)}\right], \quad (7c)$$

where ν is Poisson's ratio. We assume $\nu = 1/3$ in the numerical calculation. The shape of the crystal with the edge dislocation $l\|x$, $b\|y$ is shown in Fig. 2(b).

III. KINEMATICAL THEORY

In the kinematical theory of x-ray diffraction, the incident beam is diffracted only once by the atoms. We totally neglect the effect of multiple diffraction. The incident beam is a plane wave with a wave vector $\mathbf{k}_i$, which lies in the xy plane as shown in Fig. 1. We consider the case of a reflection topograph, where the principal diffraction planes are (100) planes. The angle of incidence with respect to the diffraction planes is denoted by θ. Then $\mathbf{k}_i$ is given by

$$\mathbf{k}_i = (-k\sin\theta, -k\cos\theta, 0), \quad (8)$$

where k is the absolute value of $\mathbf{k}_i$ related to the wavelength of x rays, λ, by

$$\lambda = \frac{2\pi}{k}. \quad (9)$$

As we consider only the elastic scattering, the wave number of the diffracted wave is k.

We denote the coordinate of the observation point P as

$$\mathbf{p} = (x_p, y_p, z_p) \quad (10)$$

in calculating a reflection topograph. The standard formalism of the kinematical theory assumes that $|\mathbf{p}|$ is much larger than the size of the crystal and the scattered wave is approximated by a plane wave. However, we take a more exact formalism that the diffracted beam is a sum of spherical waves whose origins are each atom. The amplitude of the diffracted beam is given by

$$A = A_i \cdot f \sum_j Q_j \exp[i\mathbf{k}_i \cdot \mathbf{r}_j]\frac{\exp[ik|\mathbf{p}-\mathbf{r}_j|]}{|\mathbf{p}-\mathbf{r}_j|}, \quad (11)$$

where A_i is the amplitude of the incident beam, Q_j the polarization factor, and f the atomic scattering factor. The position of the jth atom, $\mathbf{r}_j$, in the perfect crystal is given by Eq. (2) and that in the dislocated crystal by Eq. (6). The polarization factor is given by

$$Q_j = \epsilon_0 \cdot \epsilon_j, \quad (12)$$

where ϵ_0 and ϵ_j are polarization vectors for the incident and scattered x rays, respectively. The effect of Q_j is negligible in the case of the normal incidence.

For simplicity we assume $A_i = 1$, $Q_j = 1$, and $f = 1$ in Eq. (11), so that Eq. (11) is simplified to
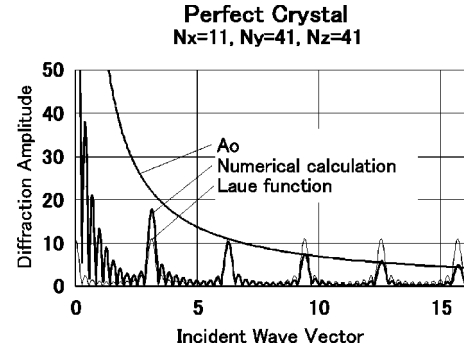
FIG. 3. Comparison of the numerically calculated amplitude of x-ray diffraction from a perfect crystal with $N_x = 11$ and $N_y = N_z = 41$ with the Laue fucntion [Eq. (15)] and A_0 [Eq. (32)].

$$A(k) = \sum_j \exp[i\mathbf{k}_i \cdot \mathbf{r}_j]\frac{\exp[ik|\mathbf{p}-\mathbf{r}_j|]}{|\mathbf{p}-\mathbf{r}_j|}. \quad (13)$$

We will use Eq. (13) together with Eq. (2) or (6) for the numerical calculation of the amplitude and intensity of the diffracted x rays.

IV. X-RAY DIFFRACTION FROM PERFECT CRYSTALS

In this section, we calculate the x-ray diffraction from the perfect crystal.

We examine reflection topographs in the case of normal incidence. The direction of the incident x rays is antiparallel to the x axis, the diffraction planes are (100), and the angle of incidence is $\theta = 90°$. The unit of position and length is $a = 1$.

The thick solid line in Fig. 3 shows the amplitude spectrum of diffracted x-ray beam from a perfect crystal calculated numerically with $N_x = 11$, $N_y = 41$, and $N_z = 41$ at $\mathbf{p} = (100,0,0)$. The spectrum of the incident beam is assumed to be white. Diffraction peaks appear at $k = \pi$, 2π, and so on. The height of the peaks increases with N_x, while their width decreases with N_x.

Figure 3 indicates that the diffraction peaks appear in accordance with the Bragg condition

$$m\lambda = 2a\sin\theta, \quad (14)$$

where m is an integer.

The line shape of the diffraction peaks in the kinematical theory is usually given by the Laue function

$$L_x = \left|\frac{\sin(N_x ka)}{\sin(ka)}\right|. \quad (15)$$

The line shape given by Eq. (15) is plotted in Fig. 3 as a thin solid line. The positions of the zero points and peaks calculated from Eqs. (13) and (15) agree quite well, but the amplitudes of the diffraction peaks do not agree. The variation of the peak values will be discussed in Sec. VII.

According to Eq. (15), the main peaks occur at $\sin(ka) = 0$. This is equivalent to the Bragg condition, Eq. (14). The first main peak is located at
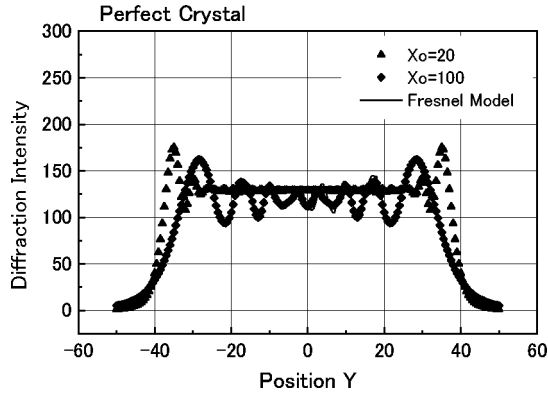
FIG. 4. X-ray topographs of a perfect crystal with $N_x = 11$ and $N_y = N_z = 81$ at two distances $x_0 = 20$ and 100. The solid line represents the Fresnel diffraction from a knife edge at $x_0 = 100$.

$$k_1 = \frac{\pi}{a}. \tag{16}$$

The zero points nearest to k_1 are located at

$$k = k_1 \pm \Delta k, \tag{17}$$

where

$$\Delta k = \frac{\pi}{N_x a}. \tag{18}$$

The integrated intensity of the diffraction peak around $k = k_1$ is defined by

$$I = \int_{k_1 - \Delta k}^{k_1 + \Delta k} |A(k)|^2 dk. \tag{19}$$

We expect that the value of I depends on the position of the observation point.

The integrated diffraction intensity of a model crystal is calculated at various observation points within a plane parallel to the yz plane, using Eqs. (2), (13), and (19). We call the set of the integrated diffraction intensity as the x-ray topograph hereafter. As shown in Fig. 1, the center of the x-ray topograph corresponding to the center of the crystal is located at $P_0 = (x_0, y_0, z_0)$. The line OP_0 lies on the xy plane as well as the incident x ray and makes an angle of θ with the negative direction of the y axis. In the case of the normal incidence, we have $y_0 = z_0 = 0$, and x_0 becomes the distance from the center of the crystal to P_0.

Figure 4 shows x-ray topographs of a perfect crystal with $N_x = 11$, $N_y = 81$, and $N_z = 81$. The observation points in Fig. 4 are taken along a line parallel to the y axis given by

$$\mathbf{p} = (x_0, y, 0). \tag{20}$$

The triangles in Fig. 4 represent the x-ray topograph at a distance of $x_0 = 20$, and the diamonds represent the x-ray topograph at a distance of $x_0 = 100$. In both cases the x-ray topographs are symmetrical with respect to $y = 0$.

In the x-ray topograph at $x_0 = 20$, the diffraction intensity is almost constant for $-25 < y < 25$, oscillates several times
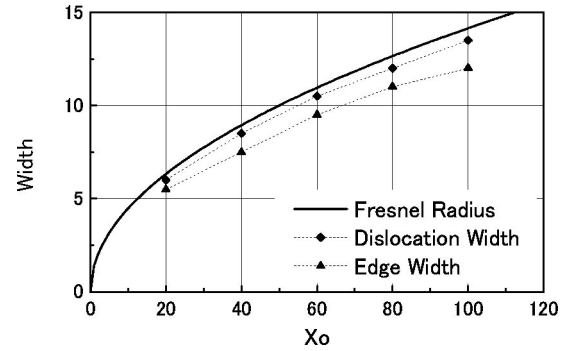

FIG. 5. The widths of the crystal edge Δy and the dislocation image on the x-ray topographs W_d. The solid line represents the radius of the first Fresnel zone r_1.

with increasing y, reaches a maximum at $y_m = 35.0$, and then decreases monotonically to zero. The oscillation is related to the edge of the crystal, whose position is defined by

$$y_e = \frac{N_y a}{2} \tag{21}$$

from Eq. (4). For the crystal in Fig. 4 we have $y_e = 40.5$. The edge width of the crystal in the x-ray topograph is characterized by

$$\Delta y = y_e - y_m. \tag{22}$$

For the x-ray topograph at $x_0 = 20$ we have $\Delta y = 5.5$. The x-ray topograph at $x_0 = 100$ has a wider oscillating region and a longer period of oscillation than that at $x_0 = 20$. Its maximum occurs at $y_m = 28.5$ and we have $\Delta y = 12.0$.

Calculations for various values of N_x, N_y, and N_z indicate that Δy depends on x_0 but not on the size of the crystal. When N_y is varied, for example, the oscillating part of the x-ray topograph is shifted along with y_e so that Δy is kept constant. Figure 5 shows the relation between Δy and x_0.

V. X-RAY DIFFRACTION FROM DISLOCATED CRYSTALS

In this section, we calculate x-ray topographs of the dislocated crystals. We restrict ourselves to the case of normal incidence, $\theta = 90°$. The size of the crystals is $N_x = 11$, $N_y = 81$, and $N_z = 81$, unless specified otherwise.

Figure 6 shows the x-ray topograph of a dislocated crystal with a screw dislocation $l \| x$, $b \| x$ which lies along the x axis (No. 1 in Table I). The diffraction intensity has been calculated in two directions parallel to the y and z axes centering at $P_0 = (20, 0, 0)$, using Eqs. (6), (13), and (19). As the direction of the incident x rays is antiparallel to the x axis, the projection of the dislocation on the topograph is a point at $y = 0$ and $z = 0$. There is a profound dip at the center of the topograph in Fig. 6 accompanied by two peaks on both sides of the dip. The positions of the peaks are -6.0 and $+6.0$. As the feature is the same for both y and z directions, the dip is expected to be circular in shape with a radius of $r = 6.0$ on the two-dimensional x-ray topograph. The diffraction intensity at the center of the dip is zero. The diffraction intensity
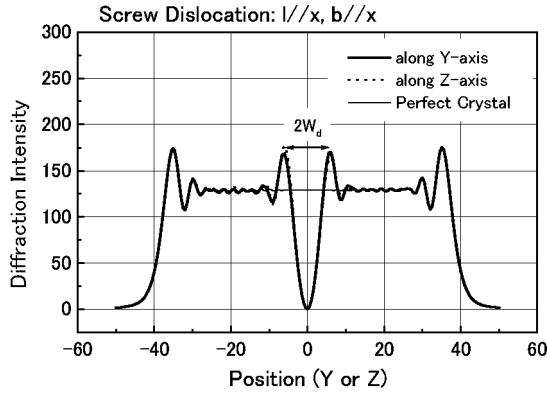
FIG. 6. X-ray topographs of a crystal with a screw dislocation $l \| x$, $b \| x$ at a distance of $x_0 = 20$ in y and z directions. The full width of the dislocation image is indicated by $2 W_d$.

for $y < -20$ and $y > 20$ is the same as that of the perfect crystal, including the oscillation of the intensity at the edge of the crystal. If the direction of the Burgers vector of the screw dislocation is opposite to x ($l \| x$, $b \| -x$), we get a similar x-ray topograph. Therefore the image of the screw dislocations $l \| x$, $b \| x$ and $l \| x$, $b \| -x$ on the x-ray topograph is localized around the position of the dislocation, and the effect of the screw dislocation is to reduce the diffraction intensity down to zero.

Figure 7 shows the x-ray topograph of a dislocated crystal with an edge dislocation $l \| x$, $b \| y$. The projected position of the dislocation on the topograph is at $y = 0$ and $z = 0$, but except for a small dip at $z = -6$ and a small peak at $z = 6$, the topograph is almost the same as that of the perfect crystal and shows no clear sign of the dislocation. We get similar results for dislocated crystals with an edge dislocation $l \| x$, $b \| -y$, with an edge dislocation $l \| x$, $b \| z$, and with an edge dislocation $l \| x$, $b \| -z$.

The x-ray topographs of dislocated crystals with a screw dislocation $l \| y$, $b \| y$, with a screw dislocation $l \| y$, $b \| -y$, with a screw dislocation $l \| z$, $b \| z$, and with a screw dislocation $l \| z$, $b \| -z$ are the same as that of the perfect crystal and show no sign of the dislocation at all.

Figure 8 shows the x-ray topograph of a dislocated crystal with an edge dislocation $l \| y$, $b \| x$. The projection of the
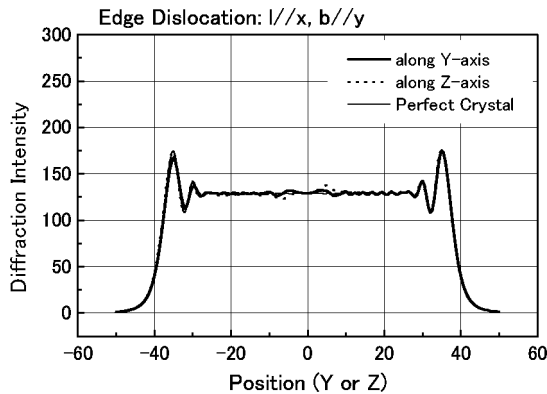

FIG. 7. X-ray topographs of a crystal with an edge dislocation $l \| x$, $b \| y$ at a distance of $x_0 = 20$ in the y and z directions.
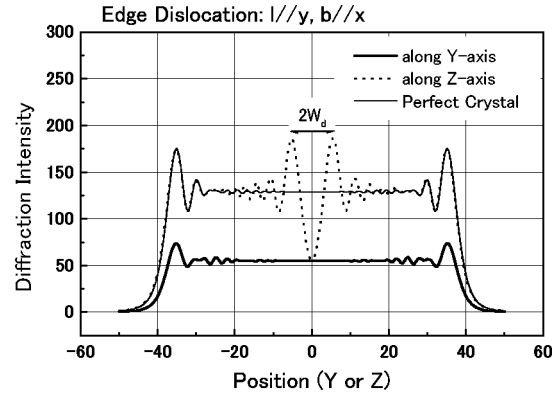

FIG. 8. X-ray topographs of a crystal with an edge dislocation $l \| y$, $b \| x$ at a distance of $x_0 = 20$ in the y and z directions.

dislocation on the topograph is a line along the y axis. The topograph along the z axis shows a dip at $z = 0$ and two peaks at $z = -5.5$ and 5.5. The topograph along the y axis, on the other hand, has a small but constant value for $-20 < y < 20$ which coincides with the dip value of the topograph along the z axis. Hence the image of the dislocation on the two-dimensional x-ray topograph is a trench along the y axis which is parallel to the dislocation direction. The depth of the trench is 46% of the perfect-crystal value. If the direction of the Burgers vector is opposite to x ($l \| y$, $b \| -x$), we get a similar x-ray topograph.

We get similar dislocation image in the topographs of crystals with an edge dislocation $l \| z$, $b \| x$ and with an edge dislocation $l \| z$, $b \| -x$. The only difference lies in that the dislocation image appears along the z axis.

Figure 9(a) shows the x-ray topograph of a dislocated crystal with an edge dislocation $l \| y$, $b \| z$. The projection of the dislocation on the topograph is a line along the y axis. The image of the dislocation is a trench along the y axis similar to the case of $l \| y$, $b \| x$. If the direction of the Burgers vector is opposite to z ($l \| y$, $b \| -z$), however, we get a different image of the dislocation as shown in Fig. 9(b). The topograph along the z axis shows a peak at $z = 0$ accompanied by two dips at $z = -5$ and 4.5. The image of the dislocation is a ridge along the y axis in this case. The depth of the trench in Fig. 9(a) is 61% of the perfect-crystal value, while the height of the ridge in Fig. 9(b) is 146% of the perfect-crystal value.

We get similar dislocation image in the topographs for a pair of crystals with an edge dislocation $l \| z$, $b \| y$ and with an edge dislocations $l \| z$, $b \| -y$. The only difference lies in that the dislocation image appears along the z axis.

The results of calculations for the dislocated crystals are summarized in Table I.

VI. X-RAY TOPOGRAPHS OF SOLID HELIUM

The x-ray topographs of solid helium have been taken using the synchrotron radiation (SR) x-ray beam at the Photon Factory of the National Laboratory of High Energy Physics.[11] The geometry of the SR x-ray topography for solid helium is shown in Fig. 10. As it is a transmission geometry and the window behind the sample chamber containing the
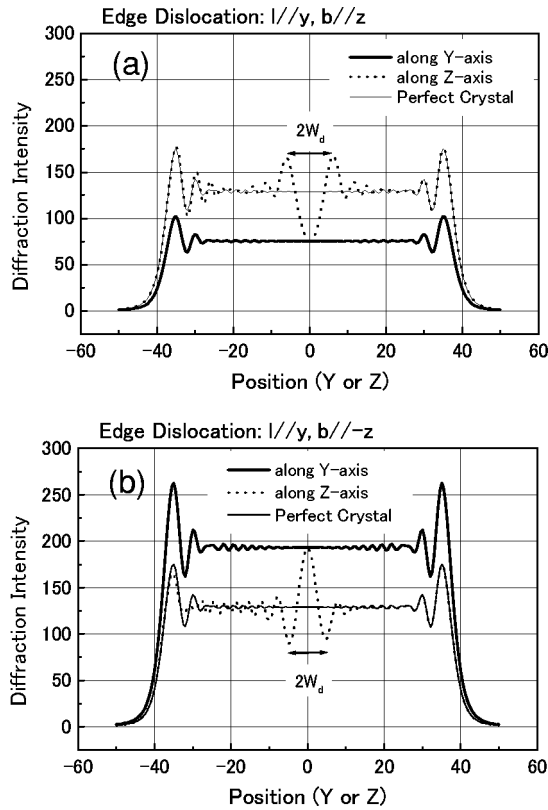
FIG. 9. X-ray topographs of (a) a crystal with an edge dislocation $l\|y$, $b\|z$ and (b) a crystal with an edge dislocation $l\|y$, $b\|-z$ at a distance of $x_0=20$ in the y and z directions.

helium crystal has an aperture of approximately $\pm20°$, the angle of incidence is limited to $\theta_B\leq10°$. The distance from the center of the sample chamber to the nuclear plate, which takes the topograph, is $x_0=80$ mm. The hcp ^{4}He crystal grown at a constant pressure of 4.0 MPa has a molar volume of 20.5 cm^3/mol. The lattice constants are $a=0.360$ nm and $c=0.588$ nm. The spacings, d, of a few diffraction planes of the hcp ^{4}He crystal are listed in Table II.[16] The most frequently observed diffraction spot is of $1\bar{1}01$ type, because it has a relatively large spacing and the biggest multiplicity (i.e., the number of equivalent spots) of 12. From the Bragg
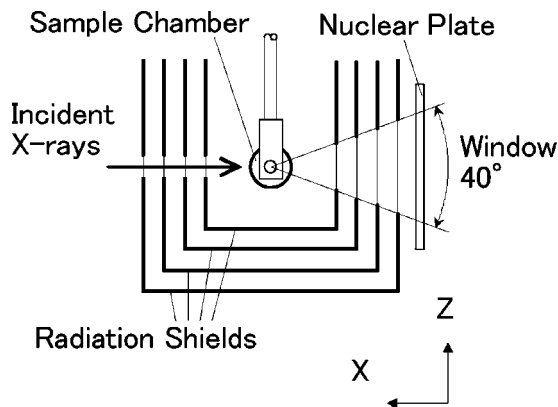

FIG. 10. The geometry of synchrotron-radiation x-ray topography for solid helium. Topographs are taken on the nuclear plate.

TABLE II. Diffraction spots from the hcp helium crystal.

Miller index	Lattice spacing (nm)	Multiplicity
$1\bar{1}00$	0.312	6
0002	0.294	2
$1\bar{1}01$	0.275	12
$1\bar{1}02$	0.214	12
$11\bar{2}0$	0.180	6
$1\bar{1}03$	0.166	12

condition with $\theta_B=10°$ and $d=0.275$ nm, the typical wavelength of diffracted x rays is determined to be

$$\lambda=0.096 \text{ nm}. \tag{23}$$

Figure 11 shows three x-ray topographs of an hcp ^{4}He crystal taken simultaneously on a nuclear plate. The Miller indices are assigned to be $0\bar{1}1\bar{1}$, $0\bar{1}10$, and $0\bar{1}11$. The overall parallelogram shape of the topographs assures that the observed region of the sample is a single crystal. White and black bands represent the subboundaries in the crystal. A remarkable feature is that the contrast and width of the subboundaries appear differently in each topograph. Their widths range between 30 and 200μm on the topographs. The subboundaries P, Q, and R are planes perpendicular to the basal plane of the hcp ^{4}He crystal and approximately making an angle of 60° with each other.[11] The region S is bright in all the topographs.
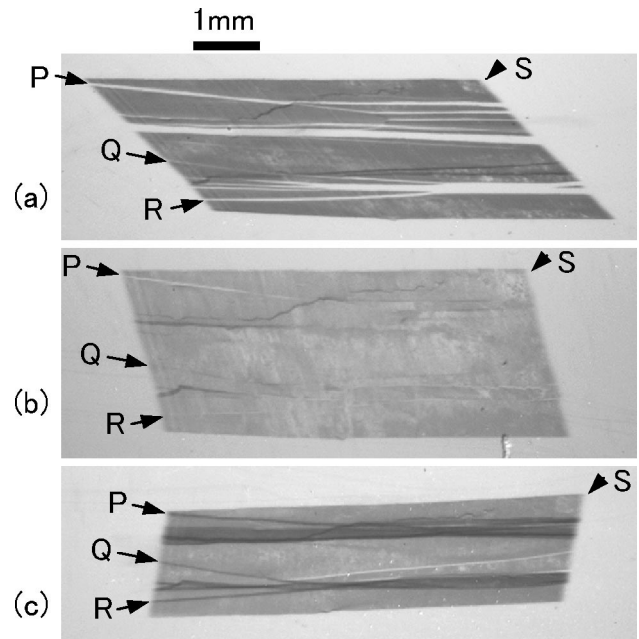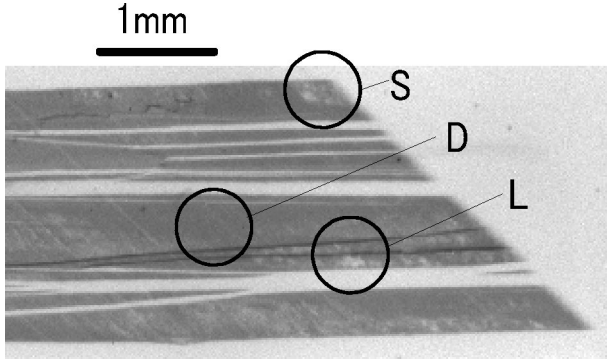

FIG. 11. X-ray topographs of an hcp ^{4}He crystal. (a) $0\bar{1}1\bar{1}$ diffraction, $\theta_B=9.8°$, (b) $0\bar{1}10$ diffraction, $\theta_B=10.1°$, and (c) $0\bar{1}11$ diffraction, $\theta_B=8.0°$. P, Q, and R indicate subboundaries, and S indicates a region of bright contrast.

FIG. 12. Enlarged x-ray topograph of $0\bar{1}1\bar{1}$ diffraction.

An enlarged x-ray topograph of Fig. 11(a) is shown in Fig. 12. Apart from the subboundaries there are uniformly dark regions D and spotty bright regions L and S.

VII. DISCUSSION

The origin of the oscillation of intensity near the edge of the crystal is the same as the Fresnel diffraction of light wave from a knife edge.[17] Let us calculate the Fresnel diffraction of monochromatic ($\lambda=2$) and parallel light wave incidnt on a knife edge located at $y=y_e$. The incident direction is parallel to the x axis. The intensity of light at $\mathbf{p}=(x_0,y,0)$ is given by

$$I_F=\frac{1}{2}\left[\left\{U\left(\frac{y-y_e}{\sqrt{x_0}}\right)-\frac{1}{2}\right\}^2+\left\{V\left(\frac{y-y_e}{\sqrt{x_0}}\right)-\frac{1}{2}\right\}^2\right], \quad (24)$$

where $U(x)$ and $V(x)$ are the Fresnel integrals defined by

$$U(x)=\int_0^x\cos^2\left(\frac{\pi u^2}{2}\right)du, \quad (25a)$$

$$V(x)=\int_0^x\sin^2\left(\frac{\pi u^2}{2}\right)du. \quad (25b)$$

Equation (24) is calculated for $x_0=100$ and $y_e=40.5$, multiplied by a factor of $N_x^2=121$, and plotted in Fig. 4 as a solid line, which agrees with the x-ray topograph at $x_0=100$ very well except for the center region ($y<10$).
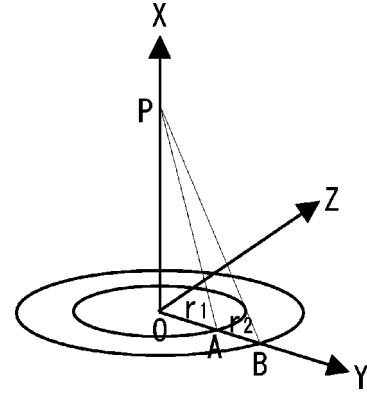
We next introduce the radius of the first Fresnel zone, r_1. In Fig. 13, the point P is on the x axis at $OP=x_0$ and the point A is on the y axis with $OA=r_1$, where r_1 is defined to be the radius of the first Fresnel zone when

$$AP-OP=\frac{\lambda}{2}. \quad (26)$$

The distance AP is given by

$$AP=\sqrt{OP^2+OA^2}=\sqrt{x_0^2+r_1^2}\approx x_0+\frac{r_1^2}{2x_0}. \quad (27)$$

The last equality is valid when $x_0\gg r_1$. From Eqs. (26) and (27) we obtain

FIG. 13. The definition of the radius of the first Fresnel zone r_1 and that of the second Fresnel zone r_2.

$$r_1=\sqrt{\lambda x_0}. \quad (28)$$

Equation (26) means that the spherical x-ray waves which emerge from the points within the ring of radius r_1 given by Eq. (28) are in phase at the observation point P with the phase shift being less than π. On the other hand, the x-ray waves from outside the first Fresnel zone have a phase shift bigger than π.

The solid line in Fig. 5 represents r_1. By comparing Δy and r_1, the edge width in the x-ray topograph is approximately given by

$$\Delta y=0.86r_1. \quad (29)$$

We regard r_1 as a representative of the resolution of the x-ray topograph, because it is proportional to the width of the crystal edge on the x-ray topograph and it is an increasing function of λ and x_0 via Eq. (28).

In the following we call the phenomena related to the radius of the first Fresnel zone as the Fresnel model. The distance between the crystal and observation point and the wavelength of x rays play an important role in the Fresnel model.

The number of atoms in the first Fresnel zone of the model crystal is given by

$$N_1=\frac{N_x\pi r_1^2}{a^2}. \quad (30)$$

This is a measure of how many atoms are involved in the diffraction intensity at the observation point because the spherical waves from inside the first Fresnel zone interfere constructively. By replacing $|\mathbf{p}-\mathbf{r}_j|$ in Eq. (13) with x_0 and restricting the summation to the N_1 atoms in the first Fresnel zone, we obtain the contribution of the N_1 atoms to the diffraction amplitude to be

$$|A_1|=\frac{2\lambda N_x}{a^2}. \quad (31)$$

The spherical waves from inside the second Fresnel zone interfere destructively, those of the third Fresnel zone constructively, and so on. Because the contributions from the

second and higher-order Fresnel zones cancel with each other, the net effect is that the diffraction amplitude is reduced approximately to a half value of A_1,

$$|A_0| = \frac{|A_1|}{2} = \frac{\lambda N_x}{a^2}. \tag{32}$$

Equation (32) is shown as a dotted line in Fig. 3. Note that Eq. (32) does not depend on the distance x_0. The reason is that the amplitude of a spherical wave from an atom is decreased as $1/x_0$ but the number of atoms in the first Fresnel zone is increased proportional to x_0 because of Eqs. (28) and (30) and both effects cancel each other.

The width of a dislocation line image is increased as the distance from the crystal to the observation point is increased according to Eq. (28). Assuming the dislocation width to be $2r_1$ and the width of the crystal edge to be r_1, the distance x_m at which the size of the crystal, L, is equal to $4r_1$ is given by

$$x_m = \frac{(N_y a)^2}{16\lambda} = \frac{L^2}{16\lambda}, \tag{33}$$

where

$$L = N_y a \tag{34}$$

for the model crystal.

The dislocation image can be spacially resolved on the x-ray topograph when

$$x_0 \ll x_m. \tag{35}$$

In the case of $a=1$, $N_y=81$, and $\lambda=2$, we have $x_m=205$.

X-ray topographs for 18 dislocated crystals have been calculated as listed in Table I, out of which 10 cases show a dislocation image and 8 cases show no dislocation image. There is a common feature in the cases of no dislocation image that the displacement in the x direction, u, is zero. On the other hand, in those cases in which the dislocation image appears, the displacement u is not zero. In the topographs studied in Sec. V, the diffraction planes are (100) and the diffraction vector is $\mathbf{g}=[100]$. Hence, u is the component of the displacement which is parallel to the diffraction vector. We can generalize the condition that the dislocation image is observed to be

$$\mathbf{g} \cdot \mathbf{u} \neq 0, \tag{36}$$

where $\mathbf{u}$ is the displacement vector.

Out of 10 cases in which the dislocation image appears, the diffraction intensity decreases in 8 cases and increases in 2 cases. As a consequence, the diffraction intensity is expected to be lower on average in the region of the crystal with high dislocation density if different types of dislocations are equally populated.

The two cases with increasing diffraction intensity, Nos. 12 and 16 in Table I, are characterized as follows: (1) the crystal involves an edge dislocation, (2) the slip plane (i.e., the plane which contains the Burgers vector and the dislocation line) is perpendicular to the diffraction vector, and (3)
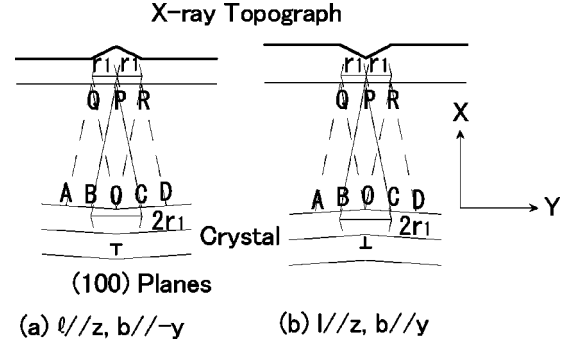

FIG. 14. Dislocation image on the x-ray topograph based on the Fresnel model. (100) planes around a dislocation line are shown in crystals with (a) an edge dislocation $l\|z$, $b\|-y$ and (b) an edge dislocation $l\|z$, $b\|y$.

when the sign of the Burgers vector is changed, the image of the dislocation becomes from an ridge to an trench.

Let us consider the case of the crystal with an edge dislocation $l\|z$, $b\|-y$ (No. 16 in Table I) in more detail based on the Fresnel model. Both sides of the (100) plane of the crystal projected on the xy plane, $ABOCD$, are bent upwards at O as shown in Fig. 14(a) with the distance OP being the same as for the perfect crystal. The first Fresnel zone corresponding to the point P on the topograph is BOC, at the center of which the dislocation is present. The phase difference between the diffracted x-ray waves from the atoms in the region BOC is decreased at P on the topograph compared with the perfect crystal because the distances BP and CP are shorter than the corresponding distances of the perfect crystal. As a result the amplitude of the diffracted x rays at P on the topograph is increased. Point Q on the topograph is distant from P by r_1. The first Fresnel zone corresponding to Q is ABO. As the line ABO is almost straight, the amplitude of the diffracted x rays at Q on the topograph is essentially the same as that for the perfect crystal. The situation is the same for point R. Hence we expect that the diffraction intensity at P is stronger than that at Q or R and that a positive image of the dislocation appears around P, whose width is approximately given by $2r_1$.

In the crystal with an edge dislocation with $l\|z$, $b\|y$ (No. 15 in Table I), on the other hand, both sides of the (100) plane, $ABOCD$, are bent downwards at O as shown in Fig. 14(b) with the distance OP being the same as for the perfect crystal. Then we expect that the diffraction intensity at P is weaker than that at Q or R and that a negative image of the dislocation appears around P.

It is evident from the discussion above that the width of the dislocation image in the Fresnel model is closely related to r_1. We define the half width of the dislocation image, W_d, to be the distance from the minimum to the peak of the x-ray topograph as indicated in Fig. 6. Figure 5 shows W_d for a crystal consisting of $N_x=11$, $N_y=161$, and $N_z=161$ atoms with a screw dislocation $b\|x$, $l\|x$ as a function of x_0. The width of the image of the crystal edge and r_1 are also shown in the figure. There is a good correlation between W_d and r_1 as expected.
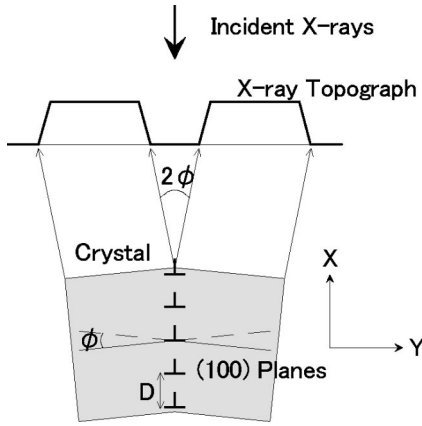
FIG. 15. A crystal with a subboundary consisting of an array of edge dislocations $l\|z$, $b\|y$ and a corresponding x-ray topograph.

The width of the dislocation image depends somewhat on the type of the dislocation as shown in Table I.

A subboundary may appear as a dark or bright band on the x-ray topograph. Let us consider a subboundary formed by an array of edge dislocations $l\|z$, $b\|y$ which are equally spaced in the x direction as shown in Fig. 15. The (100) plane in one of the subgrains is inclined with respect to the (100) plane in the other subgrain. The angle between the (100) planes of the subgrains is given by

$$\phi = \frac{b}{D}, \tag{37}$$

where D is the spacing between the dislocations. The incident x rays are antiparallel to the x axis. The Bragg condition for one subgrain is different from that of the other subgrain, so that the direction of the topograph of one subgrain is shifted from that of the other subgrain by an angle of 2ϕ and the subboundary becomes visible on the topograph.

Consequently, the subboundary appears as a band with lower diffraction intensity parallel to the z direction on the topograph similar to the image of the edge dislocation $l\|z$, $b\|y$. The width of the band is given by

$$W = 2x_0 \tan \phi + 2\Delta y, \tag{38}$$

where x_0 is the distance OP and Δy is given by Eq. (22).

On the other hand, a subboundary formed by an arrray of edge dislocations $l\|z$, $b\|-y$ appears as a band with higher diffraction intensity similar to the image of the edge dislocation $l\|z$, $b\|-y$. In this sense, an individual dislocation and a subboundary cannot be distinguished. However, the width of a subboundary can be much larger than that of a single dislocation.

Next we consider the x-ray topographs of solid helium. There are differences in the experimental and calculational conditions, such as the size of the crystal, the distance x_0, the Bragg angle, and the crystal structure, which will be discussed below.

The size of the crystal and distance from the crystal to the observation point are different between the experiment and calculation. However, the essential condition that a dislocation image can be observed in the x-ray topograph is given
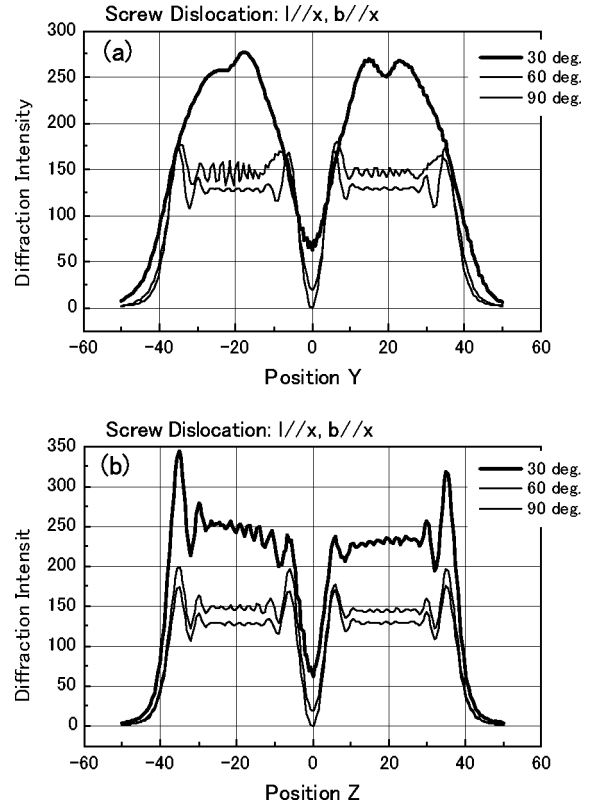

FIG. 16. Dislocation image of a screw dislocation $l\|x$, $b\|x$ at different angles of incidence.

by Eq. (35). Namely, the distance in the calculation is limited by the size of the model crystal. On the other hand, when we assume $L = 1$ mm (typical size of a subgrain) and $\lambda = 0.1$ nm for the experiment, we get $x_m = 2.5 \times 10^3$ m which is much larger than $x_0 = 80$ mm. The full width of a dislocation image in the x-ray topographs of solid helium is estimated to be

$$2W_d \approx 2r_1 = 5.5 \ \mu\text{m} \tag{39}$$

by putting $\lambda = 0.1$ nm and $x_0 = 80$ mm in Eq. (28).

The calculations in Sec. V are performed in the backreflection geometry ($\theta_B = 90°$) because of the simplicity of calculation, while the experiment is done in the transmission geometry. Figure 16 shows the x-ray topographs of a dislocated crystal with an screw dislocation $l\|x$, $b\|x$, at different angles of incidence. As θ_B is decreased from 90° to 30°, the width of the dislocation image along the y axis is increased and the minimum amplitude at $y = 0$ is increased, while the width of the dislocation image along the z direction is not changed. The variations are interpreted as the projection of the dislocation line on the yz plane is changed from a point for $\theta_B = 90°$ to a line elongated in the y direction for smaller θ_B. Thus the dislocation image can be observed in the transmission topographs as well as in the reflection topograph with a slight change in contrast.

The crystal structure affects both the types of dislocations which are formed in the crystal and the types of diffraction spots which can be observed in the x-ray diffraction experiments. The experimentally observed diffraction spots from

the hcp ^{4}He crystals are of 0002, $1\bar{1}00$, $1\bar{1}01$, and $1\bar{1}02$ types. Dislocations with Burgers vector $b=a$ are more easily formed than dislocations with $b=c$ in the hcp ^{4}He crystal, because of the lower formation energy. Basal dislocations having $b=a$ and lying in the basal plane may split into partial dislocations and form a stacking fault between them. However, it can be seen without going into such details why the dislocation image is observed in the x-ray topographs within the kinematical theory: (1) The amplitude $A(k)$ at the observation point P in the x-ray topograph is approximately given by a sum of the amplitudes of diffracted x rays from the atoms within the first Fresnel zone. (2) The atoms around a dislocation core is displaced from the atomic positions in the perfect crystal as much as the lattice spacing. As a consequence, the phase of the diffracted x rays is shifted up to 2π and the amplitude $A(k)$ at the observation point may be considerably changed from the value of the perfect crystal.

Now the image of subboundaries in Fig. 11 is explained based on the results of the calculations. The subboundaries P, Q, and R are perpendicular to the basal plane of the hcp ^{4}He crystal and consist of basal dislocations.[11] In particular, the subboundary P consists of an array of basal dislocations with an averaged Burgers vector

$$\mathbf{b}=\frac{3\mathbf{b}_1+\mathbf{b}_2}{4} \tag{40}$$

and l making an angle of $14°$ with $[01\bar{1}0]$ direction, where $\mathbf{b}_1=(a/3)[2\bar{1}\bar{1}0]$ and $\mathbf{b}_2=-(a/3)[\bar{1}2\bar{1}0]$.

We consider a basal edge dislocation with $l\|[01\bar{1}0]$ and $\mathbf{b}=\mathbf{b}_1$ here. When the diffraction vector is $[0\bar{1}10]$ and the dislocation is $l\|[01\bar{1}0]$ and $\mathbf{b}=\mathbf{b}_1$, case No. 3 in Table I is applied and no dislocation image is expected. When the diffraction vector is $[0\bar{1}1\bar{1}]$ or $[0\bar{1}11]$, the diffraction vectors can be decomposed to

$$[0\bar{1}1\bar{1}]=[0\bar{1}10]+[000\bar{1}], \tag{41a}$$

$$[0\bar{1}11]=[0\bar{1}10]+[0001]. \tag{41b}$$

The $[0\bar{1}10]$ component gives no image of the dislocation $l\|[01\bar{1}0]$ and $\mathbf{b}=\mathbf{b}_1$. The $[000\bar{1}]$ and $[0001]$ components, on the other hand, correspond to Nos. 11 and 12 in Table I giving a dislocation image of trench and ridge, respectively. Hence, the white and black contrast of the subboundaries in Figs. 11(a) and 11(c) is caused by the $[0001]$ component of the diffraction. The thin white image of the subboundary in Fig. 11(b) is probably due to the $\mathbf{b}_2$ component of the dislocations.

Apart from the subboundaries there are uniformly dark regions D and spotty bright regions L and S. The former are the regions of low dislocation density and the latter are the regions with high dislocation density, because the diffraction intensity is decreased in a region with high dislocation density as we have discussed in this section. The bright contrast in region S is caused by the dislocation image from the $[0\bar{1}10]$ component, because it is commonly observed in Figs. 11(a), 11(b), and 11(c).

We compare finally the electron diffraction described by the columnar approximation[14] with the x-ray diffraction based on the Fresnel model.

The diffraction amplitude in the columnar approximation is given by

$$A=F\sum_j \exp[2\pi i(\mathbf{g}+\mathbf{s})\cdot(\mathbf{r}_j+\mathbf{u}_j)], \tag{42}$$

where F is the atomic scattering factor for the unit cell, $\mathbf{g}$ a reciprocal lattice vector, $\mathbf{s}$ a small vector representing the difference between $\mathbf{g}$ and the diffraction vector $\mathbf{K}/2\pi$,

$$\mathbf{K}=2\pi i(\mathbf{g}+\mathbf{s}), \tag{43}$$

$\mathbf{r}_j$ the position of unit cells in the perfect crystal, and $\mathbf{u}_j$ the displacement of unit cells from $\mathbf{r}_j$ due to the dislocation. The summation is taken over a column in the direction of diffraction with the width of one unit cell. Using

$$\mathbf{g}\cdot\mathbf{r}_j=n, \tag{44}$$

where n is an integer, we obtain

$$A=F\sum_j \exp[2\pi i(\mathbf{s}\cdot\mathbf{r}_j+\mathbf{g}\cdot\mathbf{u}_j)]. \tag{45}$$

Here the higher-order term $\mathbf{s}\cdot\mathbf{u}_j$ is neglected. Dislocations can be observed when $\mathbf{g}\cdot\mathbf{u}_j$ is not zero, which is equivalent to Eq. (36).

There are differences in the experimental conditions of electron-beam and x-ray diffraction: (1) The wavelength of the electron beam is 3.7×10^{-3} nm (at 100 kV), while that of the x rays is typically 0.1 nm. (2) The electron beam can be focused on the screen, while no focusing lenses are available for x rays. (3) The electron beam is monochromatic, while the x-ray beam of synchrotron radiation has a broad spectrum.

One of the consequenses is a small value of the radius of the first Fresnel zone r_1 for the elcetron beam. As the electron beam can be focused, the distance between the sample and observation point in the electron diffraction is effectively the thickness of the sample, which is about 100 nm. The radius of the first Fresnel zone for electron is estimated to be $r_1=0.6$ nm, by substituting $\lambda=3.7\times10^{-3}$ nm and $x_0=100$ nm into Eq. (28). Because this value of r_1 is comparable to the lattice constant, the columnar approximation is valid for electron diffraction. The radius of the first Fresnel zone in the x-ray topography of solid helium, on the other hand, is 2.77μm, which is 10 000 times as big as the lattice constant. Hence the columnar approximation is not valid for x-ray diffraction and the summation in Eq. (13) should be taken not merely on a column but at least over a region which includes the first Fresnel zone.

In the electron diffraction, the columnar approximation results in stronger contrast on one side of the dislocation line than in the perfect region of the crystal. The position of the strong contrast is approximately given by the condition

$$\mathbf{s}\cdot\mathbf{r}_j+\mathbf{g}\cdot\mathbf{u}_j=0, \tag{46}$$

because $\mathbf{s}\neq0$ for the perfect region of the crystal and the strain field around the dislocation line leads to $\mathbf{g}\cdot\mathbf{u}_j<0$ on one side and $\mathbf{g}\cdot\mathbf{u}_j>0$ on the other side of the dislocation line. In the x-ray diffraction with broad spectrum, on the other hand, there is always a wavelength in the spectrum at which $\mathbf{s}=0$. Hence the condition, Eq. (46), does not cause any change in contrast. Rather the curvature of the lattice planes in the first Fresnel zone changes the phase of diffracted x rays from different atoms, and the contrast is increased only when the phase difference between them is decreased.

As discussed already there are only two cases of decreased phase difference. In other cases the phase difference is increased and the contrast around the dislocation is weaker than the perfect crystal.

VIII. CONCLUSION

X-ray topographs of perfect crystals and dislocated crystals have been calculated within the kinematical theory. It turned out from the calculations for perfect crystals that the calculation of x-ray topographs was closely related to the Fresnel diffraction in the theory of optics. The calculated edge profile of the crystal was the same as the knife edge profile of the Fresnel diffraction and its width was proportional to the radius of the first Fresnel zone.

The dislocation image on the x-ray topograph was found to be a circle, a ridge, or a trench depending on the type of dislocation and diffraction condition. Its radius or width was comparable to the radius of the first Fresnel zone. A necessary condition for a dislocation image to appear on the x-ray topograph was derived that the displacement vectors of atoms around the dislocation line had a component parallel to the diffraction vector. The diffraction intensity of the dislocation image was in most cases smaller than that of the perfect region in contrast to the columnar theory in which the dislocation image was always a region with higher diffraction intensity.

The Fresnel model was applied to the experiments of the x-ray topography of solid helium and the width of the dislocation image was estimated to be 5.5 μm. The white and black contrast of the subboundaries appearing on the x-ray topographs of solid helium with different Miller indices were explained in terms of the trench and ridge images of the edge dislocations based on the calculation. Thus some of the properties of dislocations in solid helium can be extracted from observation of the subboundaries in the x-ray topographs of solid helium. For example, change of the configuration of subboundaries would give us information on the motion of dislocations. When individual dislocations are identified in the x-ray topographs, we will be able to investigate their density, distribution, shape, motion, and many other properties.

*Electronic address: iwasa.izumi@fujixerox.co.jp

[1] B. K. Tanner, *X-ray Diffraction Topography* (Pergamon Press, New York, 1976).

[2] D.S. Greywall, Phys. Rev. B **15**, 2604 (1977).

[3] I. Iwasa, J. Phys. Soc. Jpn. **56**, 1635 (1987).

[4] S.M. Heald, D.R. Baer, and R.O. Simmons, Phys. Rev. B **30**, 2531 (1984).

[5] N. Sullivan, G. Deville, and A. Landesman, Phys. Rev. B **11**, 1858 (1975).

[6] I. Iwasa, K. Araki, and H. Suzuki, J. Phys. Soc. Jpn. **46**, 1119 (1979).

[7] J.R. Beamish and J.P. Franck, Phys. Rev. Lett. **47**, 1736 (1981).

[8] H. Suzuki, J. Phys. Soc. Jpn. **35**, 1472 (1973).

[9] H. Suzuki, J. Phys. Soc. Jpn. **42**, 1865 (1977).

[10] I. Iwasa, N. Saito, and H. Suzuki, J. Phys. Soc. Jpn. **52**, 952 (1983).

[11] I. Iwasa, H. Suzuki, T. Suzuki, T. Nakajima, I. Yonenaga, H. Suzuki, H. Koizumi, Y. Nishio, and J. Ota, J. Low Temp. Phys. **100**, 147 (1995).

[12] J. Wilks, *The Properties of Liquid and Solid Helium* (Clarendon Press, New York, 1967).

[13] H. Suzuki, I. Iwasa, and T. Nakajima, Jpn. J. Appl. Phys., Suppl. **26**, Suppl. 405 (1987).

[14] P.B. Hirsch, A. Howie, and M.J. Whelan, Philos. Trans. R. Soc. London, Ser. A **252**, 499 (1960).

[15] J. P. Hirth and J. Lothe, *Theory of Dislocations* (Wiley, New York, 1982).

[16] D.S. Greywall, Cryogenics **12**, 237 (1972).

[17] M. Born and E. Wolf, *Principle of Optics* (Pergamon Press, New York, 1970).